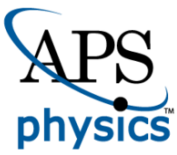

Topology, Geometry, and Mechanics of Strongly Stretched and Twisted Filaments: Solenoids, Plectonemes, and Artificial Muscle Fibers

Nicholas Charles, Mattia Gazzola, and L. Mahadevan

Phys. Rev. Lett. **123**, 208003 — Published 13 November 2019

DOI: 10.1103/PhysRevLett.123.208003

Topology, geometry and mechanics of strongly stretched and twisted filaments: solenoids, plectonemes and artificial muscle fibers

Nicholas Charles,[1] Mattia Gazzola,[2] and L. Mahadevan[3]

[1] *Paulson School of Engineering and Applied Sciences, Harvard University, Cambridge, MA 02138*
[2] *Department of Mechanical Science and Engineering, University of Illinois at Urbana-Champaign, Urbana, IL 61801, USA*
[3] *Paulson School of Engineering and Applied Sciences, Department of Physics, Department of Organismic and Evolutionary Biology, Harvard University, Cambridge, MA 02138**

(Dated: October 11, 2019)

Soft elastic filaments that can be stretched, bent and twisted exhibit a range of topologically and geometrically complex morphologies that include plectonemes, solenoids, knot-like and braid-like structures. Recently, a number of experiments have shown how to use these building blocks to create filament-based artificial muscles that use the conversion of writhe to extension or contraction, exposing the connection between topology, geometry and mechanics. Here, we combine numerical simulations of soft elastic filaments that account for geometric nonlinearities and self-contact to map out the basic structures underlying artificial muscle fibers in a phase diagram that is a function of extension and twist density. We then use ideas from computational topology to track the interconversion of link, twist and writhe in these geometrically complex physical structures to explain the physical principles underlying artificial muscle fibers and provide guidelines for their design.

The bending and twisting elastic response of soft filamentous objects is a consequence of the geometric separation of scales. This realization is at the heart of the classical Kirchhoff-Love theory [1, 2] which considers inextensible, unshearable filaments and has spawned a substantial literature [3, 4]. When such filaments are twisted strongly, they deform into plectonemic structures that consist of self-braided segments, and which have been observed across scales, from DNA to metal wires [5, 6]. The transition between the straight and plectonemic structures in inextensible filaments has been explored extensively in both a deterministic and a stochastic setting [7–10], and continues to be a topic of interest. However filaments made of soft elastomeric materials are extensible and shearable, and their study is interesting for a range of applications such as biological tissue mechanics, soft robotics etc. Amongst the simplest behaviors that harnesses these modes of deformation is the controlled transition between straight filaments and tightly coiled helical shapes (solenoids), originally observed in textiles [11], quantified experimentally in elastomers [12], and then rediscovered in the context of heat-driven artificial muscles [13]. These energy harvesting devices rely on the conversion of twist and bend into extension [14–16], as solenoids untwist and stretch. Here we consider the interplay between topology, geometry and mechanics in strongly stretched and twisted filaments to explore the range of morphologies seen and their functional consequences.

We describe a filament by a centerline position vector $\bar{\boldsymbol{x}}(s,t) \in \mathbb{R}^3$ ($s \in [0, L_0]$ is the material coordinate of the rod of rest length L_0 at time t), while the orientation of its cross-section is defined by an initially orthonormal triad associated with the director vectors $\bar{\boldsymbol{d}}_i(s,t), i = 1,2,3$, where $\bar{\boldsymbol{d}}_3(s,t)$ is normal to the material cross-section of the filament. Then, the transformation of the body-fixed frame (quantities without overbar) to the lab-fixed frame (quantities with overbar) can be written in terms of the rotation matrix $\boldsymbol{Q}(s,t) = \{\bar{\boldsymbol{d}}_1, \bar{\boldsymbol{d}}_2, \bar{\boldsymbol{d}}_3\}^{-1}$ (see Fig. 1a).

In general, the centerline tangent $\partial_s \bar{\boldsymbol{x}} = \bar{\boldsymbol{x}}_s$ does not point along the normal to the cross-section $\bar{\boldsymbol{d}}_3(s,t)$. The deviation between these vectors characterizes local extension and shear $\boldsymbol{\sigma} = \boldsymbol{Q}(\bar{\boldsymbol{x}}_s - \bar{\boldsymbol{d}}_3) = \boldsymbol{Q}\bar{\boldsymbol{x}}_s - \boldsymbol{d}_3$ (Fig. 1a), and is the basis of the Cosserat rod theory [3], that allows us to include all six modes of deformation at every cross-section (mathematically, this is associated with the dynamics on the full Euclidean group $SE(3)$). The restriction to the Kirchhoff theory corresponds to the case $\boldsymbol{\sigma} = 0$, i.e. the normal to the cross-section is also the tangent to the centerline, with $\bar{\boldsymbol{x}}_s - \boldsymbol{d}_3 = 0$.

Since many soft materials are close to being incompressible (i.e. the shear modulus is much smaller than the bulk modulus), we assume the filament material to be incompressible. Then, if $e = |\bar{\boldsymbol{x}}_s|$ is the elongation factor and A is cross-sectional area, Ae is constant. This allows us to use a simple materially linear constitutive law that is a reasonable approximation to both neo-Hookean and Mooney-Rivlin materials (see [17] and SI for validation and [18–20] for alternative approaches [43]).

Then, we may write the linear and angular momentum balance equations as [3, 4, 17]

$$\begin{aligned}
\rho A \cdot \partial_t^2 \bar{\boldsymbol{x}} =& \partial_s \left(\frac{\boldsymbol{Q}^T \boldsymbol{S}\boldsymbol{\sigma}}{e} \right) + e\bar{\boldsymbol{f}} \\
\frac{\rho \boldsymbol{I}}{e} \cdot \partial_t \boldsymbol{\omega} =& \partial_s \left(\frac{\boldsymbol{B}\boldsymbol{k}}{e^3} \right) + \frac{\boldsymbol{k} \times \boldsymbol{B}\boldsymbol{k}}{e^3} + \left(\boldsymbol{Q}\frac{\bar{\boldsymbol{x}}_s}{e} \times \boldsymbol{S}\boldsymbol{\sigma} \right) \\
&+ \left(\rho \boldsymbol{I} \cdot \frac{\boldsymbol{\omega}}{e} \right) \times \boldsymbol{\omega} + \frac{\rho \boldsymbol{I}\boldsymbol{\omega}}{e^2} \cdot \partial_t e + e\boldsymbol{c}
\end{aligned}$$

where ρ is the material density, $\bar{\boldsymbol{\omega}} = \mathrm{vec}(\partial_t \boldsymbol{Q}^T \boldsymbol{Q})$ is

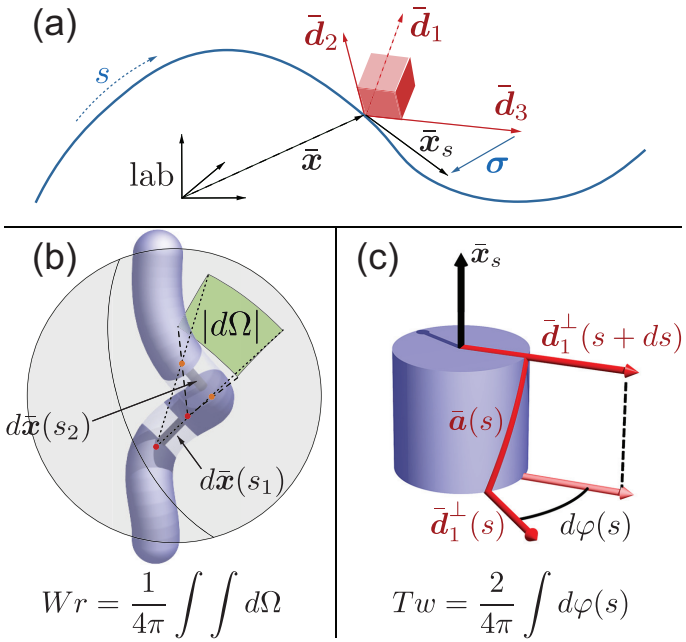

FIG. 1. Geometry and topology of soft extensible filaments. **(a)** The filament centerline $\bar{\boldsymbol{x}}(s,t)$ and local orthogonal frame $\{\bar{\boldsymbol{d}}_1, \bar{\boldsymbol{d}}_2, \bar{\boldsymbol{d}}_3\}$. Shear and extension are defined by the vector $\boldsymbol{\sigma} = \boldsymbol{Q}\bar{\boldsymbol{x}}_s - \boldsymbol{d}_3$, while curvature and twist are defined by the vector $\mathbf{k} = \text{vec}(\mathbf{Q}'\mathbf{Q}^{\mathbf{T}})$. **(b)** Writhe ($Wr$) equals the centerline's average oriented self-crossing number, computed in terms of the integral of the solid angle $d\Omega$ determined by the infinitesimal centerline segments $\bar{\boldsymbol{x}}(s_1)$ and $\bar{\boldsymbol{x}}(s_2)$ (left-handed intersections are negative). **(c)** Twist (Tw) is the integral of the infinitesimal rotations $d\varphi$ of the auxiliary curve $\bar{\boldsymbol{a}}$ around $\bar{\boldsymbol{x}}_s$. Here the vector $\bar{\boldsymbol{a}}$ traced out by $\bar{\boldsymbol{d}}_1^{\perp}$ (i.e., the projection of $\bar{\boldsymbol{d}}_1$ onto the normal-binormal plane) is shown in red while the curve associated with $-\bar{\boldsymbol{d}}_1$ is shown in yellow (see Fig. 2). For a closed curve $Lk = Tw + Wr$, where Lk (link) is the average oriented crossing number of $\bar{\boldsymbol{x}}(s)$ with $\bar{\boldsymbol{a}}(s)$.

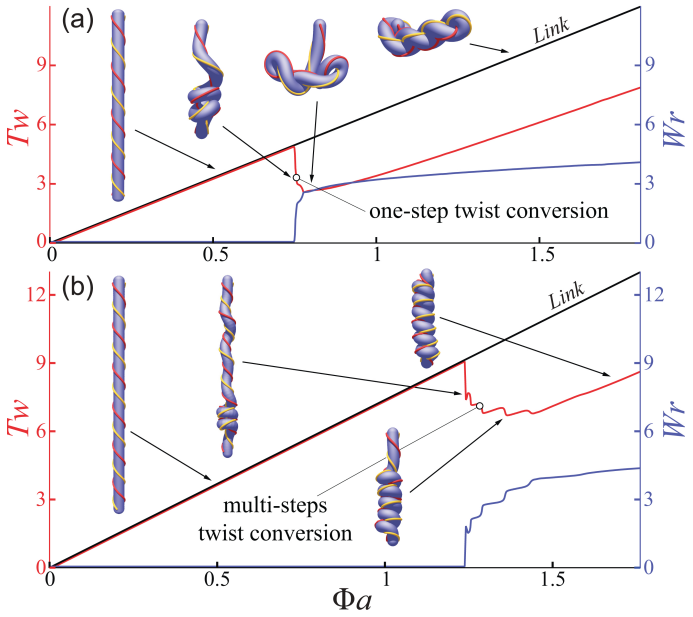

FIG. 2. Variation of the link, twist and writhe as a function of the dimensionless twist density Φa (a is filament radius in rest configuration). **(a)** To replicate the experimental observations in [12], we use a constant vertical load $F{\approx}25F_C$ to produce a plectoneme ($F_C{=}\pi^2 EI/L_0^2$ is buckling force for an inextensible rod (see Movie S1 and [35]). **(b)** We repeat the simulation with $F{\approx}90F_C$, stretching the filament to deformed length $L{\approx}1.16L_0$. Increased stretching leads to an overall similar conversion of twist to writhe leading to tightly packed solenoidal structures (See Movie S2 and SI for plots of filament energy). Simulation settings (SI): length $L_0{=}1$ m, $a{=}0.025L_0$, Young's modulus $E{=}1$ MPa, shear modulus $G{=}2E/3$, $\boldsymbol{S}{=}\text{diag}(4GA/3, 4GA/3, EA)$ N, $\boldsymbol{B}{=}\text{diag}(EI_1, EI_2, GI_3)$ Nm^2.

the local angular velocity, $\bar{\boldsymbol{k}} = \text{vec}(\partial_s \boldsymbol{Q}^T \boldsymbol{Q})$ is the local strain vector (of curvatures and twist), $\boldsymbol{S}$ is the matrix of shearing and extensional rigidities, $\boldsymbol{B}$ is the matrix of bending and twisting rigidities, and $\boldsymbol{f}, \boldsymbol{c}$ are the body force density and external couple density (see SI or [17] for details).

To follow the geometrically nonlinear deformations of the filament described by the equations above, we employ a recent simulation framework [17], wherein the filament is discretized in a set of $n+1$ vertices $\{\bar{\boldsymbol{x}}_i\}_{i=0}^{n}$ connected by edges $\bar{\boldsymbol{e}}^i = \bar{\boldsymbol{x}}_{i+1} - \bar{\boldsymbol{x}}_i$, and a set of n frames $\{\boldsymbol{Q}^i\}_{i=0}^{n-1}$. The resulting discretized system of equations is integrated using an overdamped second order scheme, reducing the dynamical simulation to a quasi-static process, and accounting for self-contact forces, internal viscous forces and the dynamic modification of the filament geometry and stiffness (SI and [17] for details [44]) while ignoring friction.

To track the knot-like structures that form when the stretched and twisted filament can contact itself, we take advantage of the CFW theorem [26, 27]: *Link* (Lk) = *Twist* (Tw) + *Writhe* (Wr). Here, link is the oriented crossing number (or Gauss linking integral) of the centerline and auxiliary curve $\bar{\boldsymbol{a}}(s)$ (Fig. 1) averaged over all projection directions [28], writhe is the link of the centerline with itself [29], and twist denotes the local rotation of the auxiliary curve about the centerline. In a discrete setting, we compute writhe, link and twist of the filament modeled as an open ribbon following [30], as illustrated in Fig. 1 (see the SI for details).

When inextensible filaments are stretched and twisted, a range of localized and self contacting structures arise, and have been well studied in both a deterministic and stochastic setting [9, 10, 31–34]. For highly stretched and twisted filaments, the phase space of possibilities is much richer, and in particular a new morphological phase associated with tightly coiled helices (solenoids) appears [11, 12]. To characterize these morphologies, we simulate twisting a filament clamped at one end and prestretched by a constant axial load, finding that the resulting buckled state changes according to the magnitude of the load. We first use an axial load ∼25 times the critical compressive buckling force of a corresponding inextensible

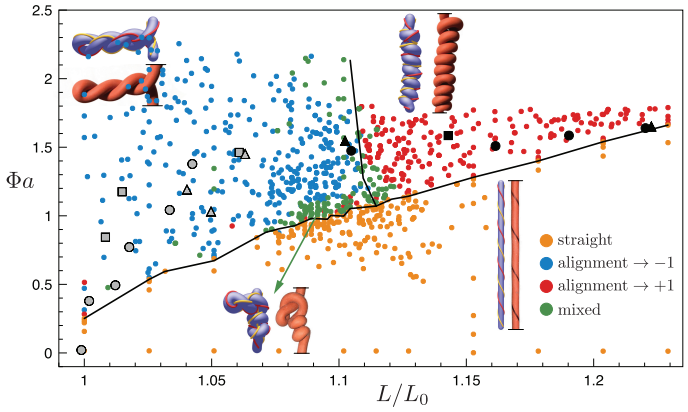

FIG. 3. Morphological phase space. We simulate a filament prestretched to L/L_0 by a constant axial load and twisted by an angle Φa, as in Fig. 2. By computing centerline relative alignment in neighboring loops, we find four phases: straight, plectoneme, solenoid and plectoneme-solenoid combinations. Plectoneme alignment ≈ -1, solenoid alignment ≈ 1 and transition configuration alignments approach 0 (dark green). For $L/L_0 \gtrsim 1.1$ solenoids are preferred. We expect Φ_{critical} to scale linearly with L/L_0 at high extension, in agreement with this plot. Our results agree qualitatively with experiments [12] (shown in black dots, see SI for details). Hollow symbols denote plectoneme transitions while solid points denote solenoid transitions; different shapes correspond to different filament parameters (SI). Simulation settings (SI): L_0=1 m, a=0.025L_0, E=1 MPa, G=2E/3, $\boldsymbol{S}$=diag($4GA/3, 4GA/3, EA$) N, $\boldsymbol{B}$=diag(EI_1, EI_2, GI_3) Nm^2.

filament $F_C = \left(\pi^2 EI\right)/L_0^2$. In Fig. 2a, denoting by a the filament rest configuration radius, we show that when a critical dimensionless twist density Φa is reached, the filament becomes unstable to bending, leading to the formation of a plectoneme, converting twist to writhe; occasionally the plectoneme can partially untie itself by slipping a loop over an endpoint, allowing link to escape the system (Fig. S3). In Fig. 2b, we repeat the simulation but quadruple the stretching strain and see that at a critical value of Φa, the filament again becomes unstable to bending, but now leads to a qualitatively different equilibrium configuration: a tightly coiled helical solenoid. We note that substantial prestretch is the crucial prerequisite for solenoid formation, while shearing is found to be unimportant (see SI for details). While both plectonemes and solenoids convert twist to writhe in steps, they are otherwise quite different. Plectonemes lead to braids made of oppositely chiral helices, while solenoids lead to a single compact helix. Furthermore, a plectoneme loop converts much more twist to writhe than a solenoid does as it coils up (Fig. 2). However the tightly-coiled nature of the solenoidal coil makes it more stable under stretching.

We now turn to explain the experimental observations and morphological phase diagram that span the twist density-extensional strain (Φa)-(L/L_0) phase space [12] (L is stretched filament length). Using randomly-sampled twist densities and extensions in this phase space, we classify each resulting configuration on the spectrum from plectoneme to solenoid using the average relative alignment of tangent vectors at filament segments which are adjoining in absolute coordinates but separated in material coordinates, i.e. $\text{avg}_{i=1}^{n}\left(\text{sign}(\bar{\boldsymbol{e}}^i \cdot \bar{\boldsymbol{e}}^k)\right)$ where k=argmin $(|\bar{\boldsymbol{x}}_k - \bar{\boldsymbol{x}}_i|)$ subject to $|k-i| > \frac{5na}{L_0}$ and $|\bar{\boldsymbol{x}}_k - \bar{\boldsymbol{x}}_i| < (2+\epsilon)a$, with ϵ=0.2 (empirically determined to maximize classification accuracy). Plectoneme loops involve two strands entwined in antiparallel directions (alignment$\to -1$), while segments of adjacent solenoid loops tend to lie parallel (alignment$\to 1$), and straight segments do not contribute to the average. In Fig. 3 we show four qualitatively different filament configurations: rectilinear, plectoneme, solenoid, and a mixed state with features of both plectonemes and solenoids; indeed the distinction between solenoid and plectoneme becomes blurred near the triple point. These simulations agree qualitatively with experimental observations [12], as illustrated in Fig. 3; the small quantitative discrepancy between experiments and simulations is likely due to our neglect of friction. It is worth pointing out that the region of solenoid-plectoneme coexistence can be expanded by having an active agent (for example, a DNA-binding enzyme) capable of either relaxing the internal axial tension and/or inducing excess twist in the filament locally. This allows for the formation of a plectoneme in the compressed segment, after which, upon further twisting, a solenoid forms below the lifted point (Fig. S9 and SI), with similarities to loop formation in chromosomes [36–38].

Our results also explain earlier observations [11] that describe straight-plectoneme-solenoid transitions in terms of varying twist density, and correspond to tracing horizontal and diagonal paths through the present extension-twist density phase diagram (see SI). Indeed, horizontally exiting the solenoid region in Fig. 3 to the right, by gradually displacing the lower solenoid endpoint away from the top, leads to a step-like solenoid *loss* process. We track the required force and resulting change in writhe (Fig. 4a). The solenoid remains mostly coiled, resisting stretching with a linear force-displacement relation, until a critical displacement at which it uncoils by one pitch and the process starts again. This stepwise uncoiling stems from a kinematic competition similar to solenoid formation: stretching the filament increases the energy required to maintain a constant number of coils. The simulated sawtooth force-displacement pattern agrees qualitatively with experiments [12].

We now turn to use our results to quantitatively explain a series of recent experiments on twisted fiber-based artificial muscles [13, 39–41] that exploit the connection between twist, writhe and link in a mechanical context. The basic mechanism is associated with the formation of solenoids in highly stretched filaments that are externally twisted [11, 12] - this leads to an increase in writhe,

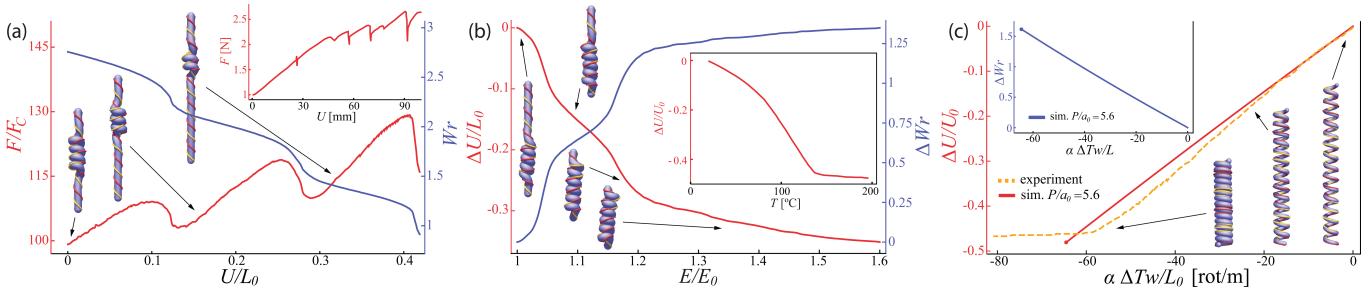

FIG. 4. Actuation of fiber-based artificial muscles that use the straight-solenoid transition. **(a)** Passive extension via solenoid loss. **(a)** We displace the unclamped end $\bar{\boldsymbol{x}}_n$ of a solenoid formed as in Fig. 3 with a load $\approx 99F_C$ load a distance ΔU in the direction $\bar{\boldsymbol{x}}_n - \bar{\boldsymbol{x}}_0$ and plot force on $\bar{\boldsymbol{x}}_n$, qualitatively reproducing experiments [12] (inset–see Movie S13). Simulation settings (SI): L_0=1 m, a=0.025L_0, E=1 MPa, G=2E/3, $\boldsymbol{S}$=diag(4GA/3, 4GA/3, EA) N, $\boldsymbol{B}$=diag(EI_1, EI_2, GI_3) Nm^2.**(b)** Active work done by changing temperature which effectively increases filament rigidity, here simply modeled by increasing the Young's modulus E of the material. This leads to the formation of a solenoidal loop in a stretched twisted filament as in Fig. 3 with a load $\approx 116\ F_C$ as E_0 increases gradually from 1 MPa, showing displacement ΔU of $\bar{\boldsymbol{x}}_n$ and increase in writhe ΔWr from initial coil writhe, reproducing experiments [13] (inset–see Movie S3). **(c)** Contraction of twisted and coiled nylon polymer muscle formed by inserting twist and annealing into helix. Filament radius doubles from initial radius a_0=0.01 m while twist decreases to keep ak_3 constant. Numerical slope and onset of self-contact (shown as point) agree closely with experimental results [13] (see SI for details). Beyond self-contact, radial growth pushes adjacent loops farther apart leading to helix elongation. Note that $\Delta Tw + \Delta Wr < 0$ in the inset; Indeed, link escapes from the free boundary due to revolution of the free filament endpoint around the helix axis, reducing the number of loops in the helix (see Fig. S7, Movies S4, S5). Simulation settings (SI): L_0=1 m, a=0.025L_0, E=30 GPa, G=2E/3, $\boldsymbol{S}$=diag(4GA/3, 4GA/3, EA) N, $\boldsymbol{B}$=diag(EI_1, EI_2, GI_3) Nm^2. Note that pitch P, α=100, number of loops and helix radius determine L_0.

causing the filament to shorten and do work against external loads. In the twisted fiber-based artificial muscles of [13, 39, 41], the externally induced twist is replaced by the use of a scalar field, temperature, that drives variations in the radius and stiffness of a pre-twisted filament and causes it to untwist, producing an equivalent increase in writhe. In Fig. 4b, we simulate this in a minimal setting by showing the effects of (temperature-induced) increase in the elastic modulus of a pre-stretched, twisted and loaded filament. To increase writhe, the solenoidal state progressively invades the straight state, lifting its lower endpoint toward the clamped end, qualitatively reproducing experimental observations of the linear actuator [13].

The sheath-run artificial muscles [39] work similarly by relying on the conversion of untwist to writhe, while the strain-programmable artificial muscles [40] generate a tensile stroke via temperature-induced differential expansion in a bilayer, that is tantamount to changing the natural curvature of a filament dynamically. Finally, the torsional actuator [41] generates torque by inserting twist into a filament and then quickly lowering the filament's intrinsic twist until it vanishes. Rather than replicate all the different variants of the fiber-based artificial muscles, here we limit ourselves to just two simple cases: the linear actuator [13], and the rotary or torsional actuator [41].

To capture the mechanics of the linear actuator, we initialize a filament with intrinsic twist and numerically anneal the filament into a uniform coil with space between adjacent loops, replicating the plastic deformation process by which twisted and coiled polymer muscles are formed. The fibers used in [13] expand radially and contract axially when heated; however, as noted quantitatively in [42], considering radial growth with fixed fiber length is sufficient. While our model applies to an isotropic filament, we can simulate anisotropic expansion-driven untwist by following the mechanical analogy in [13]: imagine winding an inextensible string around a fiber, attaching it on both fiber ends. To keep the length of the string constant, the fiber would have to untwist to expand. Mathematically, this requires ak_3 to stay constant. Hence, we prescribe a radial growth rate and continuously update the intrinsic twist $\hat{k}_3$ to keep $a\hat{k}_3$ constant [45]. For a homochiral coil the resulting untwist leads to contraction (Fig. 4), but in a heterochiral coil untwisting leads to elongation (Fig. S8, Movie S6, S7). In Fig. 4c we show the change in Wr and contraction for a simulated coil with initial inserted twist density of 2 rot/m. We scale simulated filament parameters to increase simulation efficiency and show contraction over equivalently-scaled twist density, denoting the scaling parameter by α=100. Both coils contract at the same scaled rate as experiments until adjacent loops come into contact (see SI for details of varying P/a_0). To capture the mechanics of the rotary actuator, we initialize the filament with intrinsic twist which is rapidly decreased to mimic the effect of annealing via heating. This leads to rotary motion (see section S7, movie S14).

All together, our study links topology, geometry and mechanics to explain the complex morphology of soft, strongly stretched, twisted filaments, and quantify recent experiments on artificial muscle fibers, setting the stage for the study of complex braided, knotted and twisted

filament configurations in a range of new settings.

Acknowledgements. We thank Andrew McCormick for his preliminary contributions to the project, and the UIUC Blue Waters project (OCI-0725070, ACI-1238993) (MG), the NSF EFRI C3 SoRo #1830881 (MG), the NSF CAREER #1846752 (MG), the Harvard MRSEC NSF DMR 14-20570 (LM) and Harvard BioMatter NSF DMR 33985 (LM) grants for partial financial support.

* lmahadev@g.harvard.edu

[1] G. Kirchhoff, *J. fur Mathematik* **56**, 285 (1859).
[2] A. E. H. Love, *A treatise on the mathematical theory of elasticity* (Cambridge University Press, Cambridge, 1892).
[3] S. S. Antman, *Nonlinear problems of elasticity* (Springer, New York, 2004).
[4] O. M. O'Reilly, *Modeling nonlinear problems in the mechanics of strings and rods: the role of the balance laws* (Springer, 2017).
[5] D. Beard and T. Schlick, *Journ. Chem. Phys.* **112**, 7323 (2000).
[6] J. Coyne, *IEEE Journ. of Oceanic Eng.* **15**, 72 (1990).
[7] G. H. M. Van der Heijden and J. M. T. Thompson, *Nonlinear Dynamics* **21**, 71 (2000).
[8] D. M. Stump, W. B. Fraser and K. E. Gates, *Proc. Royal Soc. A: Mathem., Phys. & Eng. Sci.* **454**, 2123 (1998).
[9] W. K. Olson and P. S. Zhang, *Methods in enzymology* **203**, 403 (1991).
[10] J. F. Marko, S. Neukirch, *Phys. Rev. E* **85**, 011908 (2012).
[11] J. W. S. Hearle and A. E. Yegin, *Journ. of the Textile Institute* **63**, 490 (1972).
[12] A. Ghatak and L. Mahadevan, *Phys. Rev. Lett.* **65**, 057801 (2005).
[13] C. Haines, N. Li, G. Spinks, A. Aliev, J. Di and R. Baughman, *Proc. Natl. Acad. Sci. USA* **113**, 11709 (2016).
[14] S. H. Kim, C. Haines, N. Li, K. J. Kim, T. J. Mun, C. Choi, J. Di, Y. J. Oh, J. P. Oviedo, J. Bykova, *et al.*, *Science* **357**, 773 (2017).
[15] S. H. Kim, H. J. Sim, J. S. Hyeon, D. Suh, G. M. Spinks, R. Baughman and S. J. Kim, *Scientific Reports* **8**, 8712 (2018).
[16] N. Atikah, L. Y. Weng, A. Anuar, C. C. Fat, I. Z. Abidin and K. S. M. Sahari, *AIP Conference Proceedings* **1883**, 020042 (2017).
[17] M. Gazzola, L. Dudte, A. McCormick and L. Mahadevan, *R. Soc. Open Sci.* **5**, 171628 (2018).
[18] J. Spillmann and M. Teschner, *ACM Transactions on Graphics (TOG)*, 63 (2007).
[19] B. Audoly, N. Clauvelin, P. T. Brun, M. Bergou, E. Grinspun, M. Wardetzky, *Journ. Comput. Phys.* **253**, 18 (2013).
[20] M. Bergou, M. Wardetzky, S. Robinson, B. Audoly, and E. Grinspun, *ACM TOG* **27**, 1 (2008).
[21] L. R. G. Treloar, *Trans. Faraday Soc.* **40**, 59 (1944)
[22] S. Reese, P. Wriggers, *Comput. Methods Appl. Mech. Eng.*, **148** (3-4), 279 (1997).
[23] O. Ahumada, M. Cocca, G. Gentile, E. Martuscelli and L. D'Orazio, *Textile Research Journ.* **74** (11), 1001 (2004).
[24] D. Clark, *et al.*, *Phys. Med. Biol.* **41** (7), 1233 (1996).
[25] O. Rodrigues, *Journal de Mathématiques* **5**, 380 (1840).
[26] F. B. Fuller, *Proc. Natl. Acad. Sci. USA* **75**, 3557 (1978).
[27] G. Calugareanu, *Rev. Math. Pures Appl.* **4**, 5 (1959).
[28] R. Ricca and B. Nipoti, *Journ. Knot Theory and its Ramifications* **20**, 1325 (2011).
[29] F. B. Fuller, *Proc. Natl. Acad. Sci. USA* **68**, 815 (1971).
[30] K. Klenin and J. Langowski, *Biopolymers* **54**, 307 (2000).
[31] S. Gerbode, J. Puzey, A. McCormick and L. Mahadevan, *Science* **337**, 1087-91 (2012).
[32] A. R. Champneys, G. H. M. Van der Heijden, J. M. T. Thompson, *SIAM Journ. Appl. Mathem.* **59**, 198 (1998).
[33] A. Goriely and M. Tabor, *Phys. Rev. Lett.* **80**, 1564 (1998).
[34] J. D. Moroz and P. Nelson, *PNAS* **94**, 14418 (1997).
[35] A. Majumdar and A. Raisch, *Nonlinearity* **27** 2841 (2014)
[36] G. Fudenberg, M. Imakaev, C. Lu, A. Goloborodko, N. Abdennur, L. Mirny, *Cell Reports* **15**, 2038-49 (2016).
[37] M. Ganji, *et al.*, *Science* **360**, 102 (2018).
[38] B. Soh, *et al.*, *Soft Matter* **14** (9), 1689 (2018).
[39] J. Mu, *et al.*, *Science* **365**, 150-155 (2019).
[40] M. Kanik, *et al.*, *Science* **365**, 145-150 (2019).
[41] J. Yuan, *et al.*, *Science* **365**, 155-158 (2019).
[42] C. Lamuta, S. Messelot and S. Tawfick, *Smart Mater. & Struct.* **27**, 055018 (2018).
[43] See Supplemental Material for further discussion of model validity, which includes Refs. [21–24].
[44] See Supplemental Material for more details about the physical model and numerical scheme, which includes Ref. [25].
[45] Note that we update *intrinsic* twist (twist of the filament in its rest configuration) $\hat{k}_3$ rather than true twist k_3, since k_3 must evolve according to the equations of motion. The filament twisting strain is defined by $k_3 - \hat{k}_3$, so the filament deforms to try to make $k_3 = \hat{k}_3$. After the onset of self-contact, radial growth pushes adjacent loops apart, lowering filament writhe and thereby forcing the filament to retwist despite an ever-increasing intrinsic twist.